Toward nodal staging of axillary lymph node basins through intradermal administration of fluorescent imaging agents

Funda Meric-Bernstam,[1,2,5] John C. Rasmussen,[3,5,*] Savitri Krishnamurthy,[4] I-Chih Tan,[3] Banghe Zhu,[3] Jamie L. Wagner,[2] Gildy V. Babiera,[2] Elizabeth A. Mittendorf,[2] and Eva M. Sevick-Muraca[3]

[1]*Department of Investigational Cancer Therapeutics, The University of Texas MD Anderson Cancer Center, Houston, TX 77030 USA*
[2]*Department of Surgical Oncology, The University of Texas MD Anderson Cancer Center, Houston, TX 77030 USA*
[3]*Center for Molecular Imaging, The Brown Foundation Institute of Molecular Medicine at the University of Texas Health Science Center at Houston, Houston, TX 77030 USA*
[4]*Department of Pathology, The University of Texas MD Anderson Cancer Center, Houston, TX 77030 USA*
[5]*These authors contributed equally to this work*
[*]john.rasmussen@uth.tmc.edu

Abstract: As part of a proof-of-concept study for future delivery of targeted near-infrared fluorescent (NIRF) tracers, we sought to assess the delivery of micrograms of indocyanine green to all the axillary lymph nodes following intraparenchymal breast injections and intradermal arm injections in 20 subjects with advanced breast carcinoma and undergoing complete axillary lymph node dissection. Lymphatic vessels and nodes were assessed *in vivo*. *Ex vivo* images demonstrated that 87% of excised lymph nodes, including 81% of tumor-positive lymph nodes, were fluorescent. Future clinical studies using microdose amounts of tumor-targeting NIRF contrast agents may demonstrate improved surgical intervention with reduced morbidity.

OCIS codes: (100.2960) Image analysis; (170.0110) Imaging systems; (170.1610) Clinical applications; (170.3880) Medical and biological imaging.

References and links

1. S. A. McLaughlin, M. J. Wright, K. T. Morris, G. L. Giron, M. R. Sampson, J. P. Brockway, K. E. Hurley, E. R. Riedel, and K. J. Van Zee, "Prevalence of lymphedema in women with breast cancer 5 years after sentinel lymph node biopsy or axillary dissection: Objective measurements," J. Clin. Oncol. **26**(32), 5213–5219 (2008).
2. S. A. Norman, A. R. Localio, S. L. Potashnik, H. A. Simoes Torpey, M. J. Kallan, A. L. Weber, L. T. Miller, A. Demichele, and L. J. Solin, "Lymphedema in breast cancer survivors: Incidence, degree, time course, treatment, and symptoms," J. Clin. Oncol. **27**(3), 390–397 (2008).
3. J. A. Petrek, R. T. Senie, M. Peters, and P. P. Rosen, "Lymphedema in a cohort of breast carcinoma survivors 20 years after diagnosis," Cancer **92**(6), 1368–1377 (2001).
4. C. Boneti, S. Korourian, Z. Diaz, C. Santiago, S. Mumford, L. Adkins, and V. S. Klimberg, "Scientific impact award: Axillary reverse mapping (arm) to identify and protect lymphatics draining the arm during axillary lymphadenectomy," Am. J. Surg. **198**(4), 482–487 (2009).
5. M. Thompson, S. Korourian, R. Henry-Tillman, L. Adkins, S. Mumford, K. C. Westbrook, and V. S. Klimberg, "Axillary reverse mapping (arm): A new concept to identify and enhance lymphatic preservation," Ann. Surg. Oncol. **14**(6), 1890–1895 (2007).
6. J. W. Han, Y. J. Seo, J. E. Choi, S. H. Kang, Y. K. Bae, and S. J. Lee, "The efficacy of arm node preserving surgery using axillary reverse mapping for preventing lymphedema in patients with breast cancer," J. Breast Cancer **15**(1), 91–97 (2012).
7. T. B. Britton, C. K. Solanki, S. E. Pinder, P. S. Mortimer, A. M. Peters, and A. D. Purushotham, "Lymphatic drainage pathways of the breast and the upper limb," Nucl. Med. Commun. **30**(6), 427–430 (2009).
8. J. E. Choi, Y. S. Jeon, S. H. Kang, and S. J. Lee, "Preservation of lymphatic drainage of arm during axillary procedure in breast cancer patients," J. Breast Cancer **12**(3), 179–185 (2009).

9. R. Ponzone, N. T. Cont, F. Maggiorotto, E. Cassina, P. Mininanni, N. Biglia, and P. Sismondi, "Extensive nodal disease may impair axillary reverse mapping in patients with breast cancer," J. Clin. Oncol. **27**(33), 5547–5551 (2009).
10. I. Bedrosian, G. V. Babiera, E. A. Mittendorf, H. M. Kuerer, L. Pantoja, K. K. Hunt, S. Krishnamurthy, and F. Meric-Bernstam, "A phase i study to assess the feasibility and oncologic safety of axillary reverse mapping in breast cancer patients," Cancer **116**(11), 2543–2548 (2010).
11. M. A. Hall, S. Kwon, H. Robinson, P.-A. Lachance, A. Azhdarinia, R. Ranganathan, R. E. Price, W. Chan, and E. M. Sevick-Muraca, "Imaging prostate cancer lymph node metastases with a multimodality contrast agent," Prostate **72**(2), 129–146 (2012).
12. M. A. Hall, K. L. Pinkston, N. Wilganowski, H. Robinson, P. Ghosh, A. Azhdarinia, K. Vazquez-Arreguin, A. M. Kolonin, B. R. Harvey, and E. M. Sevick-Muraca, "Comparison of mabs targeting epithelial cell adhesion molecule for the detection of prostate cancer lymph node metastases with multimodal contrast agents: Quantitative small-animal pet/ct and nirf," J. Nucl. Med. **53**(9), 1427–1437 (2012).
13. N. K. Tafreshi, M. M. Bui, K. Bishop, M. C. Lloyd, S. A. Enkemann, A. S. Lopez, D. Abrahams, B. W. Carter, J. Vagner, S. R. Grobmyer, R. J. Gillies, and D. L. Morse, "Noninvasive detection of breast cancer lymph node metastasis using carbonic anhydrases ix and xii targeted imaging probes," Clin. Cancer Res. **18**(1), 207–219 (2012).
14. C. H. Heath, N. L. Deep, L. N. Beck, K. E. Day, L. Sweeny, K. R. Zinn, C. C. Huang, and E. L. Rosenthal, "Use of panitumumab-irdye800 to image cutaneous head and neck cancer in mice," Otolaryngol. Head Neck Surg. **148**(6), 982–990 (2013).
15. F. Wu, M. Tamhane, and M. E. Morris, "Pharmacokinetics, lymph node uptake, and mechanistic pk model of near-infrared dye-labeled bevacizumab after iv and sc administration in mice," AAPS J. **14**(2), 252–261 (2012).
16. J. Wu, R. Ma, H. Cao, Z. Wang, C. Jing, Y. Sun, Y. Zhang, Z. Yang, R. M. Hoffman, and J. Tang, "Intraoperative imaging of metastatic lymph nodes using a fluorophore-conjugated antibody in a her2/neu-expressing orthotopic breast cancer mouse model," Anticancer Res. **33**(2), 419–424 (2013).
17. L. Sampath, W. Wang, and E. M. Sevick-Muraca, "Near infrared fluorescent optical imaging for nodal staging," J. Biomed. Opt. **13**(4), 041312 (2008).
18. T. Kitai, T. Inomoto, M. Miwa, and T. Shikayama, "Fluorescence navigation with indocyanine green for detecting sentinel lymph nodes in breast cancer," Breast Cancer **12**(3), 211–215 (2005).
19. E. M. Sevick-Muraca, R. Sharma, J. C. Rasmussen, M. V. Marshall, J. A. Wendt, H. Q. Pham, E. Bonefas, J. P. Houston, L. Sampath, K. E. Adams, D. K. Blanchard, R. E. Fisher, S. B. Chiang, R. Elledge, and M. E. Mawad, "Imaging of lymph flow in breast cancer patients after microdose administration of a near-infrared fluorophore: Feasibility study," Radiology **246**(3), 734–741 (2008).
20. D. Murawa, C. Hirche, S. Dresel, and M. Hünerbein, "Sentinel lymph node biopsy in breast cancer guided by indocyanine green fluorescence," Br. J. Surg. **96**(11), 1289–1294 (2009).
21. A. Hirano, M. Kamimura, K. Ogura, N. Kim, A. Hattori, Y. Setoguchi, F. Okubo, H. Inoue, R. Miyamoto, J. Kinoshita, M. Fujibayashi, and T. Shimizu, "A comparison of indocyanine green fluorescence imaging plus blue dye and blue dye alone for sentinel node navigation surgery in breast cancer patients," Ann. Surg. Oncol. **19**(13), 4112–4116 (2012).
22. J. R. van der Vorst, B. E. Schaafsma, F. P. Verbeek, M. Hutteman, J. S. Mieog, C. W. Lowik, G. J. Liefers, J. V. Frangioni, C. J. van de Velde, and A. L. Vahrmeijer, "Randomized comparison of near-infrared fluorescence imaging using indocyanine green and 99(m) technetium with or without patent blue for the sentinel lymph node procedure in breast cancer patients," Ann. Surg. Oncol. **19**(13), 4104–4111 (2012).
23. B. E. Schaafsma, F. P. Verbeek, D. D. Rietbergen, B. van der Hiel, J. R. van der Vorst, G. J. Liefers, J. V. Frangioni, C. J. van de Velde, F. W. van Leeuwen, and A. L. Vahrmeijer, "Clinical trial of combined radio- and fluorescence-guided sentinel lymph node biopsy in breast cancer," Br. J. Surg. **100**(8), 1037–1044 (2013).
24. M. Takeuchi, T. Sugie, K. Abdelazeem, H. Kato, N. Shinkura, M. Takada, H. Yamashiro, T. Ueno, and M. Toi, "Lymphatic mapping with fluorescence navigation using indocyanine green and axillary surgery in patients with primary breast cancer," Breast J. **18**(6), 535–541 (2012).
25. G. C. Wishart, S. W. Loh, L. Jones, and J. R. Benson, "A feasibility study (icg-10) of indocyanine green (icg) fluorescence mapping for sentinel lymph node detection in early breast cancer," Eur. J. Surg. Oncol. **38**(8), 651–656 (2012).
26. T. Sugie, T. Sawada, N. Tagaya, T. Kinoshita, K. Yamagami, H. Suwa, T. Ikeda, K. Yoshimura, M. Niimi, A. Shimizu, and M. Toi, "Comparison of the indocyanine green fluorescence and blue dye methods in detection of sentinel lymph nodes in early-stage breast cancer," Ann. Surg. Oncol. **20**(7), 2213–2218 (2013).
27. J. C. Rasmussen, S. Kwon, E. M. Sevick-Muraca, and J. N. Cormier, "The role of lymphatics in cancer as assessed by near-infrared fluorescence imaging," Ann. Biomed. Eng. **40**(2), 408–421 (2012).
28. M. L. Landsman, G. Kwant, G. A. Mook, and W. G. Zijlstra, "Light-absorbing properties, stability, and spectral stabilization of indocyanine green," J. Appl. Physiol. **40**(4), 575–583 (1976).
29. E. M. Sevick-Muraca and J. C. Rasmussen, "Molecular imaging with optics: Primer and case for near-infrared fluorescence techniques in personalized medicine," J. Biomed. Opt. **13**(4), 041303 (2008).
30. B. Zhu, J. C. Rasmussen, and E. M. Sevick-Muraca, "A matter of collection and detection for intraoperative and non-invasive fluorescence molecular imaging: To see or not to see?," Medical Physics accepted with revision (2013).

31. B. Zhu, I.-C. Tan, J. C. Rasmussen, and E. M. Sevick-Muraca, "Validating the sensitivity and performance of near-infrared fluorescence imaging and tomography devices using a novel solid phantom and measurement approach," Technol. Cancer Res. Treat. **11**(1), 95–104 (2012).
32. J. C. Rasmussen, I. C. Tan, M. V. Marshall, K. E. Adams, S. Kwon, C. E. Fife, E. A. Maus, L. A. Smith, K. R. Covington, and E. M. Sevick-Muraca, "Human lymphatic architecture and dynamic transport imaged using near-infrared fluorescence," Transl. Oncol. **3**(6), 362–372 (2010).
33. J. C. Rasmussen, I. C. Tan, M. V. Marshall, C. E. Fife, and E. M. Sevick-Muraca, "Lymphatic imaging in humans with near-infrared fluorescence," Curr. Opin. Biotechnol. **20**(1), 74–82 (2009).
34. P. E. Burrows, M. L. Gonzalez-Garay, J. C. Rasmussen, M. B. Aldrich, R. Guilliod, E. A. Maus, C. E. Fife, S. Kwon, P. E. Lapinski, P. D. King, and E. M. Sevick-Muraca, "Lymphatic abnormalities are associated with rasa1 gene mutations in mouse and man," Proc. Natl. Acad. Sci. U.S.A. **110**(21), 8621–8626 (2013).
35. E. M. Sevick-Muraca and B. Zhu, "The need for performance standards in clinical translation and adoption of fluorescence molecular imaging," Med. Phys. **40**(4), 040402 (2013).
36. S. Hirakawa, L. F. Brown, S. Kodama, K. Paavonen, K. Alitalo, and M. Detmar, "Vegf-c-induced lymphangiogenesis in sentinel lymph nodes promotes tumor metastasis to distant sites," Blood **109**(3), 1010–1017 (2006).
37. M. I. Harrell, B. M. Iritani, and A. Ruddell, "Tumor-induced sentinel lymph node lymphangiogenesis and increased lymph flow precede melanoma metastasis," Am. J. Pathol. **170**(2), 774–786 (2007).
38. K. Alitalo, T. Tammela, and T. V. Petrova, "Lymphangiogenesis in development and human disease," Nature **438**(7070), 946–953 (2005).
39. R. C. Ji, "Lymph node lymphangiogenesis: A new concept for modulating tumor metastasis and inflammatory process," Histol. Histopathol. **24**(3), 377–384 (2009).
40. T. Karpanen and K. Alitalo, "Molecular biology and pathology of lymphangiogenesis," Annu. Rev. Pathol. **3**(1), 367–397 (2008).
41. J. A. P. Leijte, I. M. C. van der Ploeg, R. A. Valdés Olmos, O. E. Nieweg, and S. Horenblas, "Visualization of tumor blockage and rerouting of lymphatic drainage in penile cancer patients by use of spect/ct," J. Nucl. Med. **50**(3), 364–367 (2009).
42. "Guidance for industry, investigators, and reviewers: Exploratory IND studies," U.S. Department of Health and Human Services, and C. D. E. R. Food and Drug Administration, eds. (2006).

1. Introduction

Tumor burden in the lymph nodes is a primary indicator utilized to clinically stage cancer progression. For early breast cancers, sentinel lymph node (SLN) biopsy provides the standard means of staging the axillary lymph nodes. When the SLN is pathologically tumor-positive or when nodal involvement in advanced breast carcinoma is known, axillary lymph node dissection (ALND), a procedure in which the axillary fat pad and lymph nodes are removed, has long been a standard-of-care. Besides the therapeutic benefit of reducing potential residual disease, ALND is also associated with several morbidities including reduced arm mobility and, in up to 15-50% of patients, lymphedema [1–3]. Axillary reverse mapping (ARM) seeks to reduce morbidity of lymph node dissection by sparing arm-draining lymph nodes that are intraoperatively identified after intradermal or subcutaneous administration of blue dye in the upper arm [4–6]. However, it has been reported that breast and arm lymphatic drainage routes are shared [7, 8], and that 11-18% of breast cancer patients with metastatic disease have at least one lymph node that drains both the breast and arm [9, 10]. Alternative, more accurate strategies are needed to identify tumor-positive and spare tumor-negative lymph nodes to reduce morbidity while conserving or improving breast cancer survival rates.

Preclinical molecular imaging studies that target cancer biomarkers for intraoperative identification of tumor-positive lymph nodes have almost all employed intravenous administrations of fluorescently labeled monoclonal antibodies [11–16]. However translation of this diagnostic imaging strategy is susceptible to false positive rates associated with (i) non-specific Fc antibody binding to the B lymphocytes, NK cells, and other cell types predominantly found in lymph nodes, and (ii) off-target biomarker expression in surrounding normal tissues. Intradermal administration of labeled antibody fragments or other targeting moieties with direct entrance into the lymphatic circulation [17] could enable reduced background and non-specific binding as well as preferential imaging of draining lymph nodes to detect tumor-positive lymph nodes, if: (i) the administration of imaging agent enables comprehensive delivery to pertinent tumor-draining lymph node basins, (ii) the imaging agent

rapidly clears from tumor-negative lymph nodes, and if (iii) the agent is retained only in cancer-positive lymph nodes.

As part of a larger research program to develop and deploy "first-in-humans" molecular imaging agents that detect cancer cells over-expressing epithelial markers within the privileged target-free environment of lymph nodes, we sought to identify whether intraparenchymal and intradermal administration of a non-specific fluorescent contrast agent in the breast and arm of breast cancer patients undergoing ALND could be used to comprehensively sample lymph nodes that are pathologically characterized in routine standard-of-care practice. Specifically, we employed an investigational near-infrared fluorescence lymphatic imaging (NIRFLI) system previously developed for non-invasive imaging of the lymph nodes and lymphatic vasculature following intradermal administration of a non-specific near-infrared fluorescent dye, indocyanine green (ICG), in order to image the ICG transport to lymph nodes draining the breasts and arms of women undergoing ALND. Unlike prior studies which successfully utilized NIRFLI to identify SLNs *in vivo* [18–26], we utilize NIRFLI to characterize, following ALND, all the *ex vivo* axillary lymph nodes for the presence of ICG. Because cancer metastasis can disrupt lymphatic flow, we report fluorescent lymph node status for both pathologically tumor-positive and tumor-negative lymph nodes.

2. Methods and materials

2.1 Study design

Under protocol approvals from the Food and Drug Administration (FDA, IND # 106,345) and Institutional Review Boards (University of Texas Health Science Center Houston and University of Texas MD Anderson Cancer Center) and following informed consent, 20 breast cancer patients (see Table 1 for demographic information), with cytologically proven axillary metastasis at presentation and scheduled for axillary lymph node dissection (ALND) at MD - Anderson, were enrolled into the study. Subjects younger than 18 years, pregnant or breast feeding, or, when of child-bearing potential, not agreeing to use a medically accepted method of contraception, or having a previous history of ipsilateral axillary surgery were excluded from the study.

After induction of anesthesia but prior to surgical skin prep, each subject received a total of twelve injections – four intraparenchymal injections in the quadrants of the breast, one sub-areolar injection, and seven intradermal injections in the ipsilateral arm as illustrated in Fig. 1. Each injection contained 25 μg of indocyanine green (ICG) in 0.1 mL of saline for a total dose of 300 μg. The ICG was prepared per manufacturer instructions by reconstituting 25mg of lyophilized ICG in 10 mL sterile water. A final concentration of 250 μg/mL was then obtained by diluting 1 mL of reconstituted ICG in 9 mL of sterile saline. Each injection site was covered with a round bandage to prevent camera saturation during imaging prior to skin prep. The subject's vital signs were monitored for 2 hours and follow up contact was made at 24 hours following the injections to screen for signs of an allergic reaction to ICG.

Immediately following ICG administration, NIRF images of the lymphatics in the arm, axilla, and breast were obtained using a custom-built imaging system described below. During imaging, the room lights as well as the surgical lamps were dimmed since their spectra overlapped with the spectral bandwidth (820-840 nm) of the imaging device. After NIRF lymphatic imaging for approximately 5 minutes, surgical procedures were carried out per standard-of-care with intermittent imaging conducted on the surgically exposed axilla.

Table 1. Demographics of female breast cancer subjects enrolled in the study.

Subject ID[a]	Age (yrs)	Weight (lbs)	BMI	Race/ Ethnicity[b]	Tumor Subtype	Positive Axillary Nodes/Total Nodes, (% Positive)	NeoCT[c] Y/N
B01	39	191	34.5	C/H	ER-, PR-, HER2-	21/31, (68%)	Y
B02	40	151	26.7	AA	ER + , PR + , HER2-	2/20, (10%)	Y
B03	47	172	27.8	C/H	ER + , PR + , ER2 +	0/16, (0%)	Y
B04	60	216	32.8	AA	ER-, PR-, HER2-	1/21,(5%)	Y
B05	42	127	22.5	AA	ER + , PR-, HER2-	0/26, (0%)	Y
B06	62	208	32.6	C	ER + , PR + , HER2-	6/14, (43%)	Y
B07	59	191	32.8	AA	ER + , PR + , HER2-	2/15, (13%	Y
B08	55	198	34.0	C	ER + , PR + , HER2-	1/33, (3%)	Y
B09	39	190	33.7	C/H	ER + , PR + , HER2 +	1/43, (2%)	Y
B10	50	148	23.2	C	ER + , PR + , HER2-	3/27, (11%)	Y
B11	29	227	39.0	AA	ER-, PR-, HER2-	15/30, (50%)	Y
B12	40	190	32.6	AA	ER-, PR-, HER2-	4/29, (14%)	Y
B13	43	155	28.3	C	ER + , PR + , HER2-	4/20, (20%)	Y
B14	56	156	25.2	C	ER + , PR-, HER2-	11/20, (55%)	Y
B15	41	125	21.5	C	ER + , PR + , HER2-	1/17, (6%)	Y
B16	46	164	30.0	A, C	ER-, PR-, HER2-	1/13, (8%)	Y
B17	75	178	30.6	C	ER + , PR + , HER2-	3/33, (9%)	N
B18	55	177	30.4	C	ER + , PR + , HER2 +	2/25, (8%)	N
B19	70	152	26.9	C	ER-, PR-, HER2-	3/26, (12%)	Y
B20	19	280	41.3	C/H	ER + , PR + , HER2 +	0/14, (0%)	Y

[a] All subjects had invasive ductal carcinoma (IDC); B20 had both IDC and inflammatory breast cancer
[b] Self reported, A = Asian; AA = African American or Black; C = Caucasian or White; H = Hispanic
[c] Neoadjuvant chemotherapy

Fig. 1. Typical injection sites in the arm and diseased breast. The solid arrows indicate the location of seven intradermal injections administered in the arm, while the dashed arrows indicate a subareolar injection and four intraparenchymal injections administered in the quadrants of the breast.

In standard-of-care ALND, the surgeon does not identify individual lymph nodes but rather resects the axillary fat pad based on anatomical boundaries. Following resection of the axillary fat pad, the individual lymph nodes were identified via palpation by the surgical pathology technician and, following lymph node isolation, placed on a paper grid for acquisition of NIRF images. Using standard pathologic procedures, the presence of nodal

tissue within each specimen was verified, and the tumor status of each lymph node was determined. Those isolated tissues which did not contain nodal tissue are identified as 'fatty specimens' in the analysis below. At no time was NIRF imaging used to influence or alter standard-of-care.

2.2 In vivo near-infrared fluorescence lymphatic imaging in the operating room

As described previously and shown in Fig. 2(a), pre- and intra-operative NIRF lymphatic imaging was accomplished using an investigational device equipped with a NIR-sensitive, military grade image intensifier and a 16-bit, frame transfer, charge coupled device (CCD) camera [27]. Images were acquired by illuminating the tissue with the diffuse output (≤ 1.9 mW/cm^2) of a 785 nm laser diode and collecting the resulting 830 nm fluorescent signal emanating from the tissue. The 785 nm excitation band and the 830 nm emission band were selected as (i) they approximately correspond to the excitation and emission peaks of dilute ICG in albumin [28], (ii) the needed laser diodes and optical filters are readily available, and (iii) the 45 nm band separation allows for clean rejection of the strongly backscattered excitation band improving the overall signal-to-noise ratio of our images [29]. The 200 ms integration time of the camera allowed the visualization of near real-time lymphatic propulsion. Prior to imaging the surgically exposed axilla, the camera head and arm were wrapped in a sterile plastic drape.

Fig. 2. Image of (a) the intraoperative imaging system used to assess lymphatic drainage of the arm and breast in the operating suite and (b) the *ex vivo* imaging system to assess the fluorescent status of the excised lymph nodes in the pathology suite.

2.3 Ex vivo near-infrared fluorescence lymph node imaging

As shown in Fig. 2(b), a 16-bit, frame transfer, electron multiplying CCD (EMCCD) camera (PhotonMax 1024, Princeton Instruments, Trenton, NJ) was mounted on a customized light tight box (95-0310-11, UVP, Upland, CA) to enable the acquisition of NIRF images of the resected lymph nodes in the pathology suite. The output of a fiber coupled, 0.9 W, 785 nm laser diode (1010-9MMF-SMA-78505-007, Intense, North Brunswick, NJ) was collimated (F240SMA-B, Thorlabs, Newton, NJ) and diffused (ED1-C50, Thorlabs, Newton, NJ) to uniformly illuminate a 4x4 grid (5.5 inch square) upon which the resected lymph nodes were placed. A 785 nm holographic notch filter (HSPF-785.0-2.0, Kaiser Optical Systems, Inc.,

Ann Arbor, MI) and an 830 nm bandpass filter (AND11333, Andover Corp., Salem, NH) rejected the backscattered excitation light, and a 28 mm Nikkor lens (Nikon, Melville, NY) focused the fluorescent signal onto the EMCCD chip. The image exposure time was set at 200 ms, and the gain of the EMCCD was adjusted as needed to visualize the excised lymph nodes without oversaturating the camera. Because lymph nodes received varying amounts of ICG, and because of the inherent dynamic range limitations of CCDs, we needed to vary gain to accurately assess presence of ICG in the lymph nodes. For reference purposes, an 830 nm LED enabled the acquisition of whole field images in the fluorescence band permitting the visualization of the lymph nodes irrespective of their fluorescent signal and without the removal of the optical filters. For the last nine subjects, a piece of fatty reference tissue from the axilla was also placed on the grid and imaged.

To evaluate noise floor of the EMCCD and thus determine a consistent threshold to determine the fluorescence status of excised lymph nodes imaged at the various gain settings used, a fluorescent solid phantom was imaged at the same instrument settings as the resected lymph nodes. The phantom consisted of six wells filled with a cured polyurethane solvent containing TiO_2, to mimic light scattering in tissues, and varying concentrations of quantum dots (QDots 800, Invitrogen, Grand Island, NY) [30]. The first well had no fluorophores, and wells 2-6 contained 0.2, 0.4, 0.6, 0.8, and 1.0 nM of QDots 800, respectively. Quantum dots were selected as (i) they are stable over long periods of time (months) whereas ICG is only stable for a few hours, and (ii) they have a small but measureable 830 nm fluorescence cross-section at 785 nm excitation [31]. From these images, a criterion for determining fluorescent status was developed as described below.

2.4 Data analysis

The preoperative images of the arm and breast were assessed for lymphatic drainage patterns, contractile lymphatic propulsion of ICG towards the axillary lymph nodes, and the presence of abnormal lymphatic structures such as tortuous or dilated vessels and fluorescent lymphatic capillaries as observed previously in lymphatic disorders [32, 33]. The intraoperative images were briefly assessed for the presence of fluorescent lymph nodes in the *in situ* axillary tissues, although this was not the objective of the protocol.

From the phantom images acquired at varying gains, we computed the contrast between the spatially averaged intensity signal with QDot800 present at concentration C, S(C), and that without QDots800 present, S(0), using the relationship, contrast = S(C)/S(0) −1. We also computed SNR(C) associated with each of the wells from the relationship, SNR(C) = 20 $\log_{10}$(S(C)/S(0)). Because contrast and SNR are directly related, we used the minimum SNR (SNR_{min}) associated with the well of the lowest QDots800 concentration with the minimum observable fluorescence level to provide a discrimination threshold for determining a fluorescent lymph node from a non-fluorescent lymph node when using the same EMCCD camera settings.

An average image of fluorescence intensity of each set of excised nodes was calculated by averaging across five images. A region of interest (ROI) was then selected around each excised specimen, and the maximum fluorescence intensity value within each ROI was determined. The SNR (defined as SNR = 20 $\log_{10}$ (S_{Fluor}/S_{Ref}) where S_{Flour} is the fluorescent tissue signal and S_{Ref} is the reference signal) of each specimen was determined. The reference signal was taken from the backscattered excitation light from the imaging grid or, when available, the fatty reference tissue. The specimen was declared fluorescently positive if its SNR was greater than SNR_{min} determined at the same camera setting using the phantoms as described above. In this manner, the criterion to determine whether a lymph node was fluorescent was consistent between patients and camera gain settings.

Technical difficulties with the *ex vivo* imager prevented assessment of the fluorescent status of the tissue specimens from subject B01. For all other subjects, the percent of the total, tumor-positive, and tumor-negative nodes, as well as the fatty specimens which were

fluorescent, was determined. Paired t-tests were performed to determine if the ICG was preferentially delivered to the tumor-positive nodes, tumor-negative nodes, or to the fatty specimens.

3. Results

3.1 Pre- and intra-operative in vivo imaging

Lymphatic vasculature and lymphatic propulsion (see Media 1 available online) toward the axilla were observed in all arms and in some breasts. As illustrated in Fig. 3, the arm lymphatics were typically linear and well-defined similar to those reported by Rasmussen *et al.* in normal subjects [32, 33]. Abnormal tortuous lymphatics (Fig. 3(a), insert) were observed in the arms of two subjects (B06 and B20), but no overtly dilated lymphatic vessels were observed in this study, as has been seen in other studies [34]. Fluorescent signals emanating from the axilla (Fig. 3(b)) were observed in all subjects, indicating the delivery of ICG to the axillary lymph nodes. The lymphatic drainage patterns observed in the breast varied by subject, with a dense network of fluorescent lymphatics being observed in one subject (B01, Fig. 3(c)), tortuous breast lymphatics observed in another (B13), and lymphatic drainage towards the sternum (Fig. 3(d)) in six subjects. However, superficial fluorescent contamination of the skin (potentially owing to the transfer of ICG from injection sites during skin prep) prevented definitive determination of the lymphatic drainage patterns in the breasts of seven subjects.
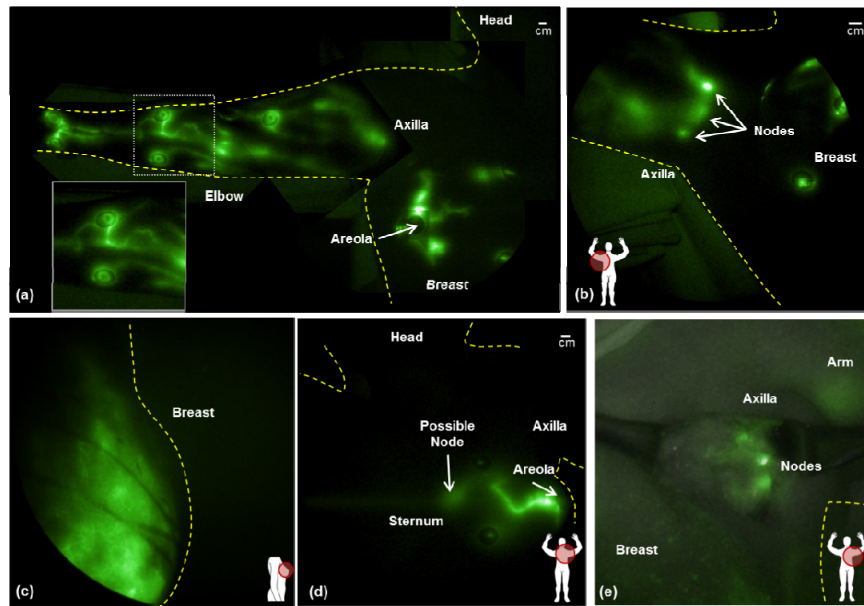

Fig. 3. (a) Image montage of lymphatic vasculature in the arm, axilla, and breast of subject (B20). While most of the lymphatics are linear and well-defined, atypical tortuous lymphatics are noted in the arm (inset box) and the drainage areas from the areola towards both the sternum and the axilla. (b) Image of axillary lymph nodes (subject B20). (c) Network of lymphatic capillaries in the upper outer quadrant of the breast in subject B01. The surgical markings are also visible as dark lines. (d) Image of lymphatic drainage towards a possible internal mammary lymph node near the sternum (subject B13). (e) Intraoperative image of fluorescent lymph nodes in the exposed axilla of subject B11. The fluorescence image is overlaid on a white light image for improved anatomical reference. Injection sites in (a), (b) and (d) are covered by round bandages.

Intraoperative imaging was performed after the axilla was exposed but prior to complete axillary resection. The time delay from the preoperative imaging to the intraoperative imaging

ranged from 28 minutes to 144 minutes, with an average delay of 92 ± 35 minutes. The length of the delay depended primarily on the surgeon and the standard-of-care surgical procedures required for patient care. Bright spots or nodes were observed within the tissues of all subjects imaged, as illustrated in Fig. 3(e); however the axillary nodes were not distinctly identified intraoperatively as per standard-of-care.

3.2 Ex vivo imaging of resected lymph nodes

The time delay between preoperative imaging and the *ex vivo* imaging of individually identified lymph nodes ranged from 82 minutes to 309 minutes, with an average delay of 188 ± 61 minutes. Figures 4(a) and 4(b) illustrate a typical color and NIRF image of resected tissue specimens on the imaging grid, as well as a piece of fatty reference tissue. As can be seen, the fluorescent intensities vary greatly from node to node and, without quantitative evaluation, the determination of fluorescent status may be subjective. Following NIRF imaging, the specimens located in each square were typically loaded into one cassette for pathologic processing. Large nodes such as the lower left node in Fig. 4(a) were divided and split across multiple cassettes per standard of practice.

Comparison of the pathologic images of the nodes indicated that the locations of the NIRF signals emanating from the lymph nodes corresponded well with the location of pathologically stained nodal tissues, as shown in Figs. 4(c)-4(h). These figures present color images of the tissue specimens on the imaging grid (Figs. 4(c) and 4(f)), their corresponding NIRF images (Figs. 4(d) and 4(g)), and images of the pathology slides (Figs. 4(e) and 4(h)) used to determine whether the specimens were lymph nodes and whether they contained tumor cells. In the first (top) lymph node in Fig. 4(d), the majority of the relatively weak fluorescent signal is emanating from the edges of the specimen. Examination of the pathologic image shows that the stained lymphatic tissues are also located primarily in the outer edges of the specimen (Fig. 4(e)). Likewise, in the second, elongated lymph node (Fig. 4(d)) two distinct depots of fluorescence are observed emanating from the opposite ends of the specimen, and pathology confirmed the presence of two distinct lymph nodes (Fig. 4(e)). In Figs. 4(g) and 4(h), the localization of the dye is again observed between the NIRF and pathologic images. In this case, however, one of the specimens (labeled as tissue 3) was not fluorescent and pathology indicated that it was not a lymph node but rather fatty tissue. It is important to note that due to the required pathologic processing, the scale and orientation of the tissue slices are not necessarily the same in the color and NIRF images which, in addition to the scatter of the fluorescent light through the fatty tissues and the intensity scaling used in the NIRF images, may account for the differences observed between the pathologic images and the fluorescent images.

3.3 Analysis of tissue fluorescence versus pathology

Figure 5 presents an image of the solid phantom with six wells filled with TiO_2 and varying concentrations of QDots 800 (Fig. 5(a)), a typical NIRF image of the phantom (Fig. 5(b)) acquired at a moderate gain, and a typical plot of the fluorescent intensity profile along a line drawn across the middle of the wells (Fig. 5(c)). While the fluorescent signal from 0.2 nM of QDots 800 was visible at this gain setting and integration time, it was associated with similar intensity as the background signals closer to the wells with higher concentration of QDots800. The intensity of fluorescent signal from the 0.4 nM well was greater than the surrounding pixels as well as those surrounding wells with higher concentration of QDots800. The 0.4 nM well was associated with a minimum contrast of 0.26 and SNR of 4.6 and provided the minimal signal from which we could confidently differentiate a true fluorescent signal. As such, the 0.4 nM well was used to calculate the minimum detectable SNR_{min} in relation to the well with no fluorophore.
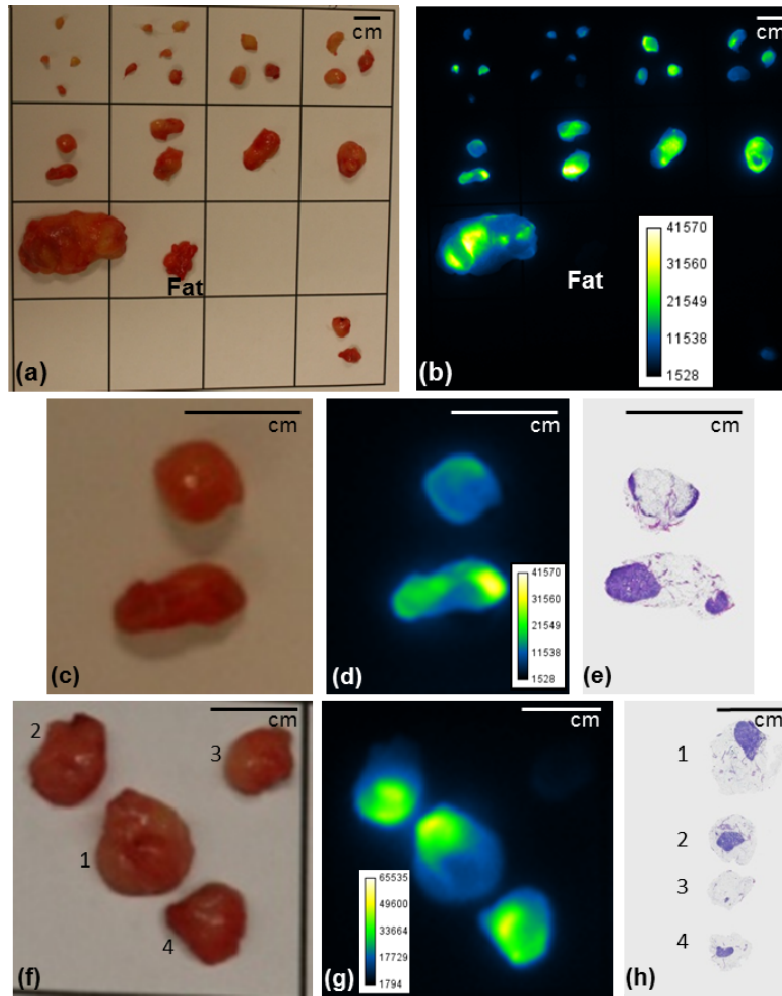
Fig. 4. (a) Color image and (b) near-infrared fluorescence image in pseudo color images of resected lymph nodes on the imaging grid (subject B19). (c) and (f) Color images of resected lymph nodes (subjects B19 and B08 respectively), (d) and (g) near-infrared fluorescence images, and (e) and (h) images of the corresponding slides from pathology. The presence of two distinct nodes in the elongated tissue sample in (c) are clearly seen in (d) and (e), and the locations of the NIRF signals also correspond well with the presence of the nodal tissues in the other stained slices (e) and (h). Note, due to pathologic processing, the scale, orientation, and cross section of the specimens in (e) and (h) are not necessarily the same as their corresponding color and NIRF images.

A plot of the minimum detectable SNR as a function of gain on the *ex vivo* imaging system is shown in Fig. 6, and illustrates the impact that variations in the gain setting can have on the SNRs of the *ex vivo*, EMCCD-based fluorescence imaging system employed with comparable data acquired using the *in vivo* ICCD-based fluorescence imaging system. Consistent with past reports, a wide range of fluorescence imaging performance may be expected from different camera systems [30, 35].

As shown in Table 2, a total of 409 tissue specimens across 19 subjects were dissected and submitted for pathologic examination. Of the 19 evaluable patients, seven (37%) were pathologically node-negative, consistent with eradication of their cytologically positive nodes
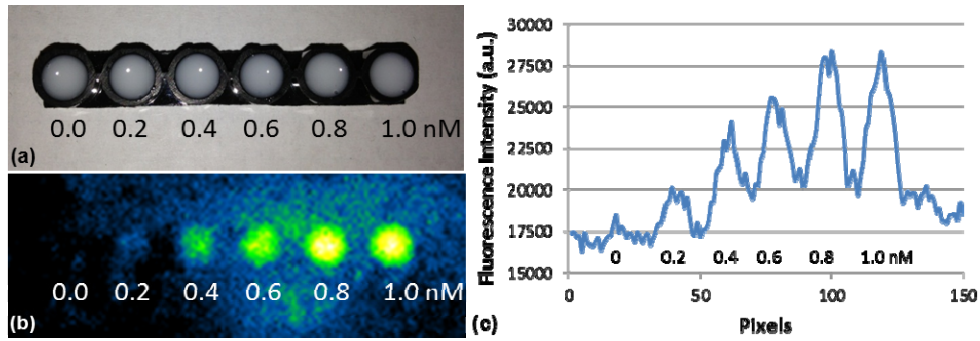
Fig. 5. (a) Image of the multi-welled phantom containing 0 to 1.0 nM Qdot 800 fluorophore. (b) Image of the typical fluorescence image detected across all the gains. (c) Fluorescence intensity profile of a line drawn across the center of the wells shown in (b). The minimum detectable signal was determined by calculating the SNR between the 0.4 nM and the 0 nM wells.
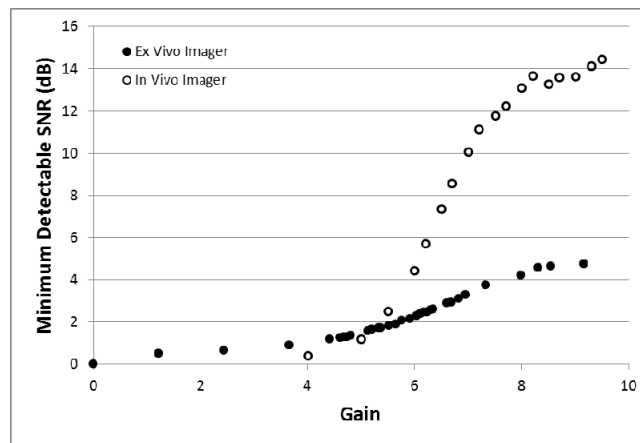

Fig. 6. Plot of the minimum detectable signal-to-noise ratio as a function of the gain for the *ex vivo* imager (EMCCD, dots) and the intraoperative imager (intensified CCD, circles).

at presentation following administration of neoadjuvant chemotherapy. Of the 409 specimens, 32 were determined to be tumor-positive lymph nodes, 338 were determined to be tumor-negative lymph nodes, 20 were determined to be fatty tissues with no lymph node tissue, and 19 specimens were excluded from the final analysis due to incomplete information which prevented conclusive determination of nodal tumor status and/or fluorescent status. The percent of the total nodes fluorescent in each subject ranged from 45% (B13) to 100% (B04, B08, B16, and B17) with 87% of the 370 total (tumor-positive and tumor-negative) lymph nodes determined to be fluorescent using the algorithm and *ex vivo* imaging device. Tumor-positive lymph nodes were found in 12 subjects, and the percent of fluorescent nodes ranged from 0% (B10) to 100% (B02, B04, B06, B07, B08, B12, B16, and B19) with 81% of all tumor-positive lymph nodes fluorescent. At least one tumor-positive node was fluorescent in 11 (92%) of the 12 subjects. The percent of fluorescent tumor-negative lymph nodes ranged from 44% (B13) to 100% (B04, B08, B16, and B17), and 88% of all tumor-negative lymph nodes were found to be fluorescent. Eight subjects had tissue specimens which were determined to be fatty tissue, with 35% determined as fluorescent. No correlation was observed between the percent of the total nodes fluorescent and age or BMI.

Subject B10 had a single tumor-positive lymph node that was not fluorescent and it was noted by the pathologist as having extranodal extension following neoadjuvant chemotherapy.

Table 2. Summary of specimen status for each subject.

Subject ID	Specimens Resected	Total Nodes (% Fluorescent)	Tumor-Positive Nodes (% Fluorescent)	Tumor-Negative Nodes (% Fluorescent)	Non-Nodal Specimens (% Fluorescent)	Unknown Specimens
B02	18	18 (89%)	2 (100%)	16 (88%)	-	-
B03	18	18 (94%)	-	18 (94%)	-	-
B04	16	16 (100%)	1 (100%)	15 (100%)	-	-
B05	24	24 (96%)	-	24 (96%)	-	-
B06[a]	12	10 (70%)	3 (100%)	7 (57%)	2 (50%)	-
B07	16	15 (67%)	1 (100%)	14 (64%)	1 (100%)	-
B08	29	28 (100%)	1 (100%)	27 (100%)	1 (100%)	-
B09	44	44 (89%)	-	44 (89%)	-	-
B10	28	21 (62%)	1 (0%)	20 (65%)	1 (0%)	6
B11	19	18 (94%)	4 (75%)	14 (93%)	1 (0%)	-
B12	31	21 (95%)	3 (100%)	18 (94%)	4 (0%)	6
B13[b]	22	20 (45%)	4 (50%)	16 (44%)	2 (0%)	-
B14	19	15 (73%)	8 (63%)	7 (86%)	-	4
B15	18	18 (94%)	-	18 (94%)	-	-
B16	14	11 (100%)	1 (100%)	10 (100%)	-	3
B17	23	23 (100%)	-	23 (100%)	-	-
B18	17	17 (88%)	-	17 (88%)	-	-
B19	24	24 (96%)	3 (100%)	21 (95%)	-	-
B20[c]	17	9 (78%)	-	9 (78%)	8 (50%)	-
Total	409	370 (87%)	32 (81%)	338 (88%)	20 (35%)	48

[a] Tortuous lymphatic in arm; [b] Tortuous lymphatic in breast; [c] Tortuous lymphatic in arm (Fig. 3(a))

Of the five other non-fluorescent, tumor-positive lymph nodes collected in the study, none were noted as having signs of neoadjuvant therapy. Similarly, of the 26 fluorescent, tumor-positive lymph nodes collected in the study, eight were noted to exhibit neoadjuvant therapy effects, while the remaining 18 had no comments noted. Approximately 30% of the fluorescent and 15% of the non-fluorescent tumor-positive lymph nodes were reported as having signs of therapy effects. The effect of therapy on the delivery of dye to the nodes remains unclear.

The average percentages of fluorescent specimens across all subjects were 86 ± 16%, 84 ± 32%, and 86 ± 16% for the total, tumor-positive, and tumor-negative lymph nodes respectively and 38 ± 44% for the fatty tissues. Including only those subjects with tumor-positive lymph nodes, a paired t-test between the percent fluorescent tumor-positive and tumor-negative lymph nodes yielded a p-value of 0.39, indicating that the tumor burden did not preferentially restrict the delivery of fluorophore to the lymph nodes; however with a *post hoc* statistical power of 7.3%, this pilot study does not have sufficient power to conclusively eliminate the effect of tumor burden on fluorophore delivery through intradermal injection. Paired t-tests between the percentage of fluorescent fatty tissues and the tumor-positive and tumor-negative nodes yielded p-values of 0.0119 and 0.0144, respectively, indicating preferential delivery to the lymph nodes.

No major adverse events were reported in this study. No patients experienced reactions to intraparenchymal or subarealor injections. Five patients developed mild erythema at the intradermal injection site, which resolved with conservative management with or without antihistamines.

4. Discussion and conclusion

4.1 Pre- and intra-operative in vivo imaging

Prior to evaluation of the fluorescent status of resected lymph nodes, this study enabled evaluation of the *contractile* function and architecture of the lymphatic vasculature draining the breast and arm. Recent histologic studies indicate that tumor-induced lymphangiogenesis results in increased numbers of tumoral and intra-nodal lymphatic vessels and increased lymphatic flow, and as a consequence, may serve as a highly sensitive and highly specific

prognostic indication of lymphatic tumor burden [36–40]. We recently demonstrated the macroscopic development of abnormal lymphatic drainage pathways consisting of tortuous, dilated collecting lymphatic vessels in a melanoma mouse model and hypothesized that their development may serve as an indication of metastatic disease [27]. However, in this study, the arm lymphatics in each subject were generally well-defined and easily observed. Of the two subjects with tortuous arm lymphatics, subject B06 had tumor-positive lymph nodes, while B20 did not. Subject B13 had a tortuous breast lymphatic vessel and tumor-positive lymph nodes; however, tortuous breast lymphatics were not observed in any of the other subjects. The upper, outer quadrant of the breast of B01 had a dense network of fluorescent lymphatic capillaries similar to that observed previously in patients with lymphedema. No overtly dilated lymphatics were observed in this study. No correlation between the arm or breast lymphatic architecture and the presence of metastatic disease was noted in this study, although additional studies are needed to determine whether the pre-surgical presence of lymphatic anomalies may indicate a predisposition to develop post-surgical lymphedema.

Axillary lymph nodes were observed *in vivo* in all subjects using the intraoperative NIRFLI system before and after the axilla had been surgically exposed. In addition, while no definitive lymph nodes were non-invasively observed near the sternum, the high incidence of lymphatic drainage towards the sternum (in 6 of the 13 subjects with no surface contamination with fluorophore) indicates that with improved and tumor-targeted contrast agents, NIRFLI may provide opportunities to non-invasively assess mediastinal and internal mammary lymph nodes which are not routinely biopsied in breast cancer patients.

The rapid subsecond acquisition of NIRF lymphatic images provides a unique opportunity to observe and quantify the movement of boluses of lymph as they are contractually propelled through the lymphatic vessels and, in a previous study, we demonstrated reduced contractile function in subjects with lymphedema [32]. While lymphatic propulsion was observed in all subjects in the current study, we were unable to assess the potential impact of the tumor on the lymphatic propulsion velocity or rate as the limited pre-surgical imaging time (~5 min) in the operating suite prevented the acquisition of sufficient propulsion data for this analysis. Future studies will be needed to further assess the effect of metastatic disease on the lymphatics and will likely need to include imaging of the contralateral arm and breast to serve as controls for better elucidation of subtle changes to the architecture and function in the ipsilateral arm and breast.

4.2 Ex vivo imaging of resected lymph nodes

In our study, ICG was successfully delivered from the injection sites in the arms and breast to the axillary lymph nodes and was present in over 87% of the resected lymph nodes, suggesting that intraparenchymal and intradermal administration of molecularly targeted agents, coupled with non-invasive imaging could be utilized to assess the status of the majority of lymph nodes in the axilla. Figure 4 illustrates the preferential uptake of the fluorescent dye within the lymph node tissues as compared to the surrounding fatty tissues. Indeed, the apparent fluorescence weakly emanating from the fatty tissues (appears blue in the NIRF images (Figs. 4(d) and 4(g))) may well be a result of the scattering of fluorescent light from the tumor through the fat and not due to the presence of dye within the fat. The fluorescent signals in fat specimens may be the result of (i) residual lymph node tissues that have been destroyed during the neoadjuvant therapy and hence are not readily apparent pathologically, (ii) small lymph nodes or lymphatic vasculature which were missed during pathologic processing, or (iii) fluorescence contamination which may have occurred during the identification of the specimens via palpation while the lymph nodes were dissected from the axillary tissues. By determining a reliable, phantom-based criterion for discriminating between fluorescent and non-fluorescent lymph nodes, we removed subjectivity in the analysis. In addition, Fig. 6 clearly shows the importance of characterizing camera systems and provides new evidence in favor of using ICCD over EMCCD based systems [30].

4.3 Analysis of tissue fluorescence versus pathology

Given that extensive tumor invasion of draining lymph nodes can alter or block lymphatic drainage pathways, we expected to visualize fewer tumor-positive lymph nodes as compared to tumor-negative lymph nodes. Indeed, it has been postulated that tumor blockage of lymphatic drainage prevents inflow of lymph into the draining lymph nodes resulting in change of normal lymphatic pathways [41]. However, in this study of advanced breast cancer patients, there appeared no difference in the percentage of resected cancer –positive and – negative lymph nodes that were fluorescent as determined from a threshold based upon SNR. The average maximum fluorescent intensity emanating from the excised specimens was selected for use in our SNR calculations, due to the large variability in the specimen size and the non-homogenous uptake of the fluorophore within the excised specimens. Other metrics, such as the average fluorescent intensity across the specimen, could be used in the SNR calculation, but would require more subjective user intervention to determine the appropriate size of the ROI due to the propensity to excise comparatively large volumes of fat along with the actual lymph node. The use of a solid, stable phantom to establish the minimum detectible SNR of the system further simplifies the determination of the fluorescent status and reduces the potential impact of the instrument settings and user interpretation on the analysis when the nodes have a weak fluorescent signal.

In our recent ARM study in which 3-5 mL of a blue dye was injected into the upper arm, blue lymph nodes were only identified in 15 of 30 subjects [10]. Herein, we successfully delivered ICG to 87% of the axillary lymph nodes following the administration of 300 μg of ICG in the arm and breast. While fluorescence was not observed in all the tumor-positive lymph nodes, at least one tumor-positive node was fluorescent in 11 of the 12 subjects with 100% of the tumor-positive nodes being fluorescent in 8 of those. These results, together with those of our prior study, in which we identified tumor-draining lymphatics and SLNs with as little as 10 μg of ICG [19], indicate that intradermal and intraparenchymal administration of microdoses of future and brighter tumor-targeting fluorescent contrast agents may be sufficient for detection of tumor-positive lymph nodes. The ability to image a microdose amount of a targeted contrast agent with sensitive devices may facilitate the use of fluorescently labeled molecular imaging agents for non-invasive nodal staging of breast cancer [42]. However, if intradermal administration of NIR agents provides insufficient delivery to the lymph nodes, improved delivery could be achieved via additional intradermal injections or through intravenous injections, although the latter could require higher doses that could reduce translation potential, due to increased safety and toxicity concerns and regulatory burden.

In summary, we have demonstrated the successful delivery of ICG to the axillary lymph nodes following intraparenchymal and intradermal injections in 19 subjects undergoing complete axillary lymph node dissection for node-positive breast cancer. The localized delivery of ICG to lymph nodes with minimal infiltration into the surrounding tissues provides future opportunities for non-invasive assessment of metastatic disease and image-guided resection of tumor-positive nodes following administration of 'first-in-human' NIRF targeted contrast agents.

Acknowledgments